## PAPER

Check for updates

# Preparation of Ag$_3$PO$_4$/α-Fe$_2$O$_3$ hybrid powders and their visible light catalytic performances

Ya Gao,[a] Haodong Ma,[b] Chengliang Han,[b] Chengmei Gui [ID] *[bc] and Chonghai Deng[b]

The inefficiency of conventional photocatalytic treatment for removing rhodamine B is posing potential risks to ecological environments. Here, we construct a highly efficient photocatalyst consisting of Ag$_3$PO$_4$ and α-Fe$_2$O$_3$ hybrid powders for the treatment of rhodamine B. Ag$_3$PO$_4$ nanoparticles (nanoparticles, about 50 nm) are uniformly dispersed on the surface of α-Fe$_2$O$_3$ microcrystals (hexagonal sheet, about 1.5 μm). The Ag$_3$PO$_4$-deposited uniformity on the α-Fe$_2$O$_3$ surface first increased, then decreased on increasing the hybrid ratio of Ag$_3$PO$_4$ to α-Fe$_2$O$_3$. When the hybrid ratio of Ag$_3$PO$_4$ to α-Fe$_2$O$_3$ is 1 : 2, the distribution of Ag$_3$PO$_4$ particles on the sheet α-Fe$_2$O$_3$ is more uniform with excellent Ag$_3$PO$_4$/α-Fe$_2$O$_3$ interface performance. The catalytic degradation efficiency of hybrids with the introduction of Ag$_3$PO$_4$ nanoparticles on the α-Fe$_2$O$_3$ surface reached 95%. More importantly, the hybrid material exhibits superior photocatalytic stability. Ag$_3$PO$_4$/α-Fe$_2$O$_3$ hybrids have good reusability, and the photocatalytic efficiency could still reach 72% after four reuses. The excellent photocatalytic activity of the as-prepared hybrids can be attributed to the heterostructure between Ag$_3$PO$_4$ and α-Fe$_2$O$_3$, which can effectively inhibit the photoelectron–hole recombination and broaden the visible light response range.

## 1. Introduction

Due to its green, high efficiency, stability and environmental friendliness, photocatalytic wastewater treatment has become one of the most promising water treatment technologies.[1–4] Nano-TiO$_2$ photocatalyst is the most widely used catalyst.[5–8] However, the application of TiO$_2$ nanomaterials is limited due to their wide band gap ($E_g$ = ~2.4 eV), low quantum efficiency and low visible light utilization rate. It is well known that Ag$_3$PO$_4$ has a band gap of 2.36 eV and can absorb visible light and ultraviolet light with wavelengths less than 525 nm. The high quantum efficiency makes Ag$_3$PO$_4$ a potential visible light catalyst.[9–13] However, the high cost and poor stability of Ag$_3$PO$_4$ limit its large-scale application. The reduction of silver ions to silver on the surface can be effectively inhibited by semiconductor compositing, metal ion doping and introducing carbon materials, and a heterostructure can be formed to improve the stability and photocatalytic activity of Ag$_3$PO$_4$. Du *et al.*[14] successfully constructed novel Z-scheme Ag$_3$PO$_4$/g-C$_3$N$_4$ heterostructures with a high photocatalytic effect. The improved photocatalytic efficiency of Ag$_3$PO$_4$/g-C$_3$N$_4$ may be attributed to the formation of Z-scheme heterostructure structure and matching valence band and conduction band. Zhouyue Wu *et al.*[15] designed and synthesized hybrid AgI@Ag$_3$PO$_4$

nanostructures for visible-light photodegradation of norfloxacin *via* a facile self-assembly formation strategy. The experimental results indicated that the AgI@Ag$_3$PO$_4$-15 sample presented the best visible-light photocatalytic performance, which was far better than that of pristine AgI and 2.96 times that of pristine Ag$_3$PO$_4$. Hematite (α-Fe$_2$O$_3$) has a narrow band gap ($E_g$ ~ 2.2 eV) and a maximum absorption wavelength of about 560 nm. It has a high utilization rate of visible light such as sunlight. Moreover, α-Fe$_2$O$_3$ is a very promising visible light catalyst with low price, environmental protection and high stability, and has a good application prospect in the field of water treatment. It has become one of the hot topics of research in recent years.[16–19]

In this study, Ag$_3$PO$_4$/α-Fe$_2$O$_3$ hybrids were prepared by hydrothermal methods. Ag$_3$PO$_4$ nanoparticles were loaded on the hexagonal α-Fe$_2$O$_3$ sheets, which greatly improved the dispersion of Ag$_3$PO$_4$ nanoparticles and increased the specific surface area of hybrids. Thus, the visible light catalytic activity of Ag$_3$PO$_4$ will be further improved. The excellent photocatalytic activity of as-prepared hybrids can be attributed to the heterostructure between Ag$_3$PO$_4$ and α-Fe$_2$O$_3$, which can effectively inhibit the photoelectron–hole recombination and broaden the visible light response range.[20–23]

## 2. Experiment section

### 2.1 Preparation of Ag$_3$PO$_4$/α-Fe$_2$O$_3$ hybrids

**Ag$_3$PO$_4$ nanopowder.** 0.25 g AgNO$_3$ and a certain amount of polyvinylpyrrolidone were dissolved in 60 mL ionized water, and the solution A was obtained by ultrasonication for 5 min. 0.19 g

[a]*Center of Analysis and Testing, Hefei University, Hefei 230601, China*
[b]*School of Energy Materials and Chemical Engineering, Hefei University, Hefei 230601, China. E-mail: guichengmei@163.com*
[c]*School of Chemistry and Chemical Engineering, Chaohu University, Hefei 230009, China*

$Na_2HPO_4$ was dissolved in 60 mL ionic water and ultrasonicated for 5 min to obtain solution B. In dark, under 75 °C with continuous stirring, solution B was added to solution A drop by drop and then the solution was left in dark for 30 min. The product was centrifuged, washed twice with deionized water and ethanol, and dried at 60 °C in a vacuum to obtain $Ag_3PO_4$ powder, as show in Fig. 1.

**α-$Fe_2O_3$ hexagonal sheets.** 1.42 g $FeCl_3 \cdot 6H_2O$ and 2 g of NaOH were dissolved in 60 mL ionic water. The solution was transferred into a kettle for hydrothermal reaction at 180 °C for 24 h. After the reaction, the product was washed with deionized water to neutral, and α-$Fe_2O_3$ was obtained, as show in Fig. 1.

**$Ag_3PO_4$/α-$Fe_2O_3$ hybrids.** 0.156 g α-$Fe_2O_3$ and a certain amount of polyvinylpyrrolidone were ultrasonically dispersed in 60 mL of water, and then a certain amount of $Ag_3PO_4$ was added to form the precursor solution. The precursor was placed in the reactor for hydrothermal reaction at 160 °C for 10 h. The reactor was then cooled to room temperature and the product was washed twice, first with deionized water then ethanol, hence obtaining the $Ag_3PO_4$/α-$Fe_2O_3$ hybrid. The hybrids with molar ratios of 1 : 4, 1 : 3, 1 : 2 and 1 : 1 of $Ag_3PO_4$ to α-$Fe_2O_3$ were also prepared, as shown in Fig. 1.

## 2.2 Photocatalytic experiments

First, 50 mg $Ag_3PO_4$/α-$Fe_2O_3$ hybrid powder was ultrasonically dispersed in 100 mL rhodamine B solution with a concentration of 5 mg $L^{-1}$. Then, the solution was magnetically stirred for 30 min in a darkroom to enable the catalyst and dye reach the equilibrium of adsorption and desorption. The photocatalytic performance was tested using a xenon lamp as the light source to simulate sunlight. 4 mL of the solution was taken every 5 min, and the absorbance of the solution was measured by UV-Vis spectrophotometer after centrifugation.

## 3. Results and discussions

The crystal phase of pure $Ag_3PO_4$, α-$Fe_2O_3$ and the $Ag_3PO_4$/α-$Fe_2O_3$ hybrid (1 : 2) was confirmed by XRD, as shown in Fig. 2.
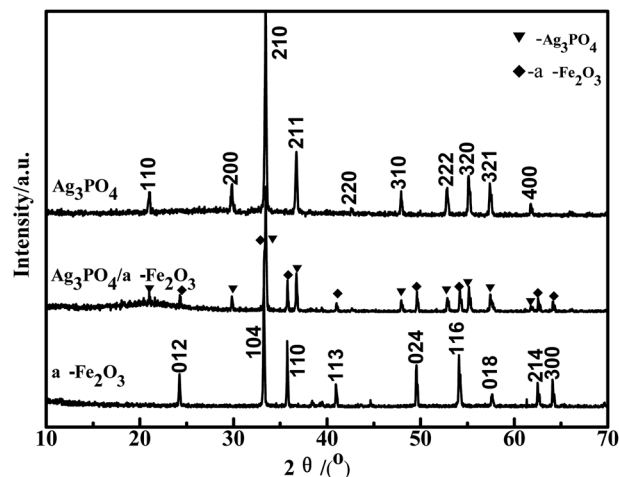


**Fig. 2** XRD patterns of $Ag_3PO_4$, α-$Fe_2O_3$ and $Ag_3PO_4$/α-$Fe_2O_3$ hybrid.

The characteristic peaks of $Ag_3PO_4$ in Fig. 2 correspond to PDF# 06-0505, which is the cubic phase silver phosphor. Diffraction peaks at 20.83°, 29.64°, 33.25°, 36.53°, 47.75°, 52.65°, 54.97°, 57.24° and 61.60° correspond to (110), (200), (210), (211), (310), (222), (320), (321), (400) crystal surfaces.[24] The diffraction peaks at 24.14°, 33.15°, 35.61°, 49.48°, 54.09°, 62.45°, 63.99° correspond to the hexagonal α-$Fe_2O_3$ (012), (104), (110), (024), (116), (214), (300) crystal planes.[25] The characteristic peaks of $Ag_3PO_4$ and α-$Fe_2O_3$ can be clearly observed in the XRD spectra of the $Ag_3PO_4$/α-$Fe_2O_3$ hybrid, which indicates that $Ag_3PO_4$ and α-$Fe_2O_3$ are successfully combined with each other. In addition, no diffraction peaks of other impurities were found on the XRD patterns, indicating that the samples had high purity. The XRD characteristic peaks of the hybrids did not change, indicating that the hybrid had no obvious effect on the crystal structure.

The morphology and structure of the catalyst can significantly affect its catalytic performance. The morphology and composition of the $Ag_3PO_4$/α-$Fe_2O_3$ hybrid photocatalyst were characterized by scanning electron microscopy (SEM) and energy dispersive spectroscopy (EDS). Fig. 3 shows the SEM
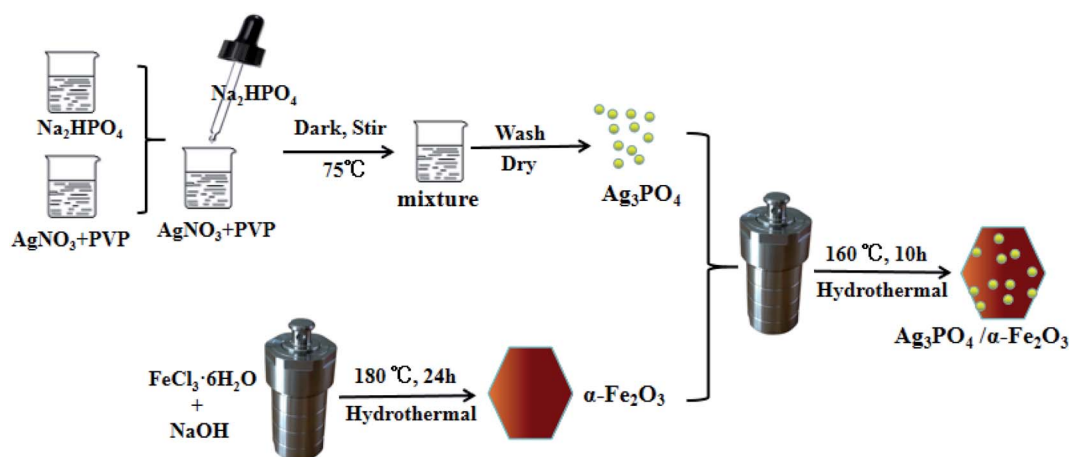


**Fig. 1** Flow chart of $Ag_3PO_4$/α-$Fe_2O_3$ preparation.
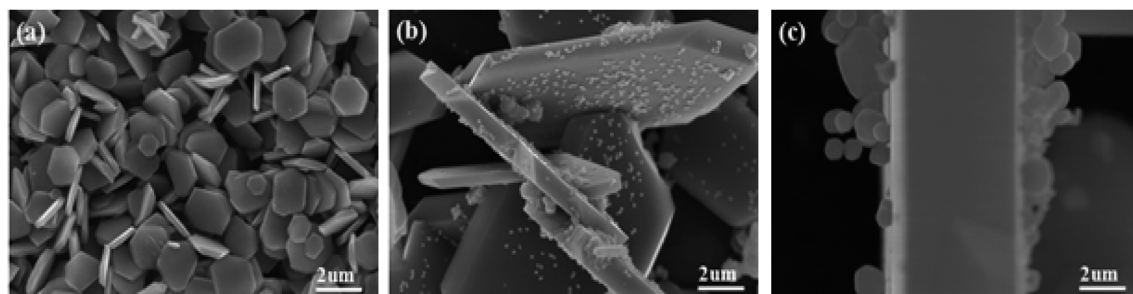
**Fig. 3** SEM images of $\alpha$-Fe$_2$O$_3$ and Ag$_3$PO$_4$/$\alpha$-Fe$_2$O$_3$ hybrid (a–c).

images of pure $\alpha$-Fe$_2$O$_3$ and Ag$_3$PO$_4$/$\alpha$-Fe$_2$O$_3$ hybrid (1 : 2). Fig. 3(a) shows $\alpha$-Fe$_2$O$_3$ is a uniform hexagonal sheet structure with a size of about 1.5 $\mu$m. In Fig. 3(b), the SEM images manifests that the small Ag$_3$PO$_4$ particles deposited on the $\alpha$-Fe$_2$O$_3$ sheet surface, with sizes of about 50 nm. From the side view of Ag$_3$PO$_4$/$\alpha$-Fe$_2$O$_3$ in Fig. 3(c), it can be seen that Ag$_3$PO$_4$ nanoparticles are closely bonded with $\alpha$-Fe$_2$O$_3$ sheets, which is conducive to the migration of photoelectric charge carriers between them to form a hybrid catalyst with high catalytic activity.[26]

Fig. 4 shows the SEM photos of Ag$_3$PO$_4$/$\alpha$-Fe$_2$O$_3$ hybrids with different proportions. It can be clearly seen from Fig. 4 that with the increase in the hybrid ratio of Ag$_3$PO$_4$ and $\alpha$-Fe$_2$O$_3$, the deposited uniformity of Ag$_3$PO$_4$ particles on $\alpha$-Fe$_2$O$_3$ surface first increased, and then decreased. When the hybrid ratio of Ag$_3$PO$_4$ and $\alpha$-Fe$_2$O$_3$ is 1 : 2, the distribution of Ag$_3$PO$_4$ particles on the sheet $\alpha$-Fe$_2$O$_3$ is more uniform and dispersed. In

addition, the Ag$_3$PO$_4$/$\alpha$-Fe$_2$O$_3$ hybrid exhibited excellent interface performance.

Fig. 5 demonstrates the EDS scan analysis spectrum of each Ag$_3$PO$_4$/$\alpha$-Fe$_2$O$_3$ hybrid photocatalyst element. It can be seen from Fig. 5(a) that the small particles protruding from the sheet structure mainly contain Ag, P, O elements, and the sheet structure is mainly composed of Fe and O elements. According to the line scanning analysis figure, the small particles on the $\alpha$-Fe$_2$O$_3$ sheet structure are Ag$_3$PO$_4$ particles, which further proves that the Ag$_3$PO$_4$/$\alpha$-Fe$_2$O$_3$ hybrid photocatalyst has been successfully prepared. Fig. 5(b) shows that O, Fe, P, and Ag elements exist in the hybrid, and from the AT% of Ag/Fe = 3.09/4.26 = 0.73 $\approx$ 0.75 (= 3/4), it can be roughly inferred that the mole ratio of Ag$_3$PO$_4$ and $\alpha$-Fe$_2$O$_3$ is 1 : 2. Because EDS results are affected by test location, only semi-quantitative analysis can be carried out.

The light absorption properties of Ag$_3$PO$_4$, $\alpha$-Fe$_2$O$_3$ and Ag$_3$PO$_4$/$\alpha$-Fe$_2$O$_3$ hybrids were analyzed by UV-Vis diffuse
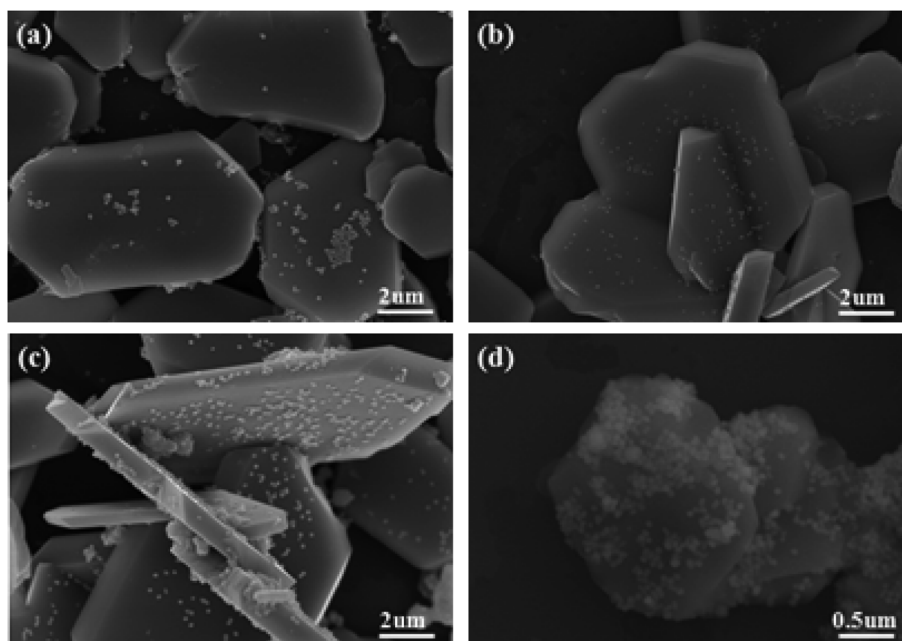


**Fig. 4** SEM photographs of Ag$_3$PO$_4$/$\alpha$-Fe$_2$O$_3$ hybrids with different proportions, the ratios of Ag$_3$PO$_4$ and $\alpha$-Fe$_2$O$_3$ are: (a)1 : 4; (b) 1 : 3; (c) 1 : 2; (d) 1 : 1.
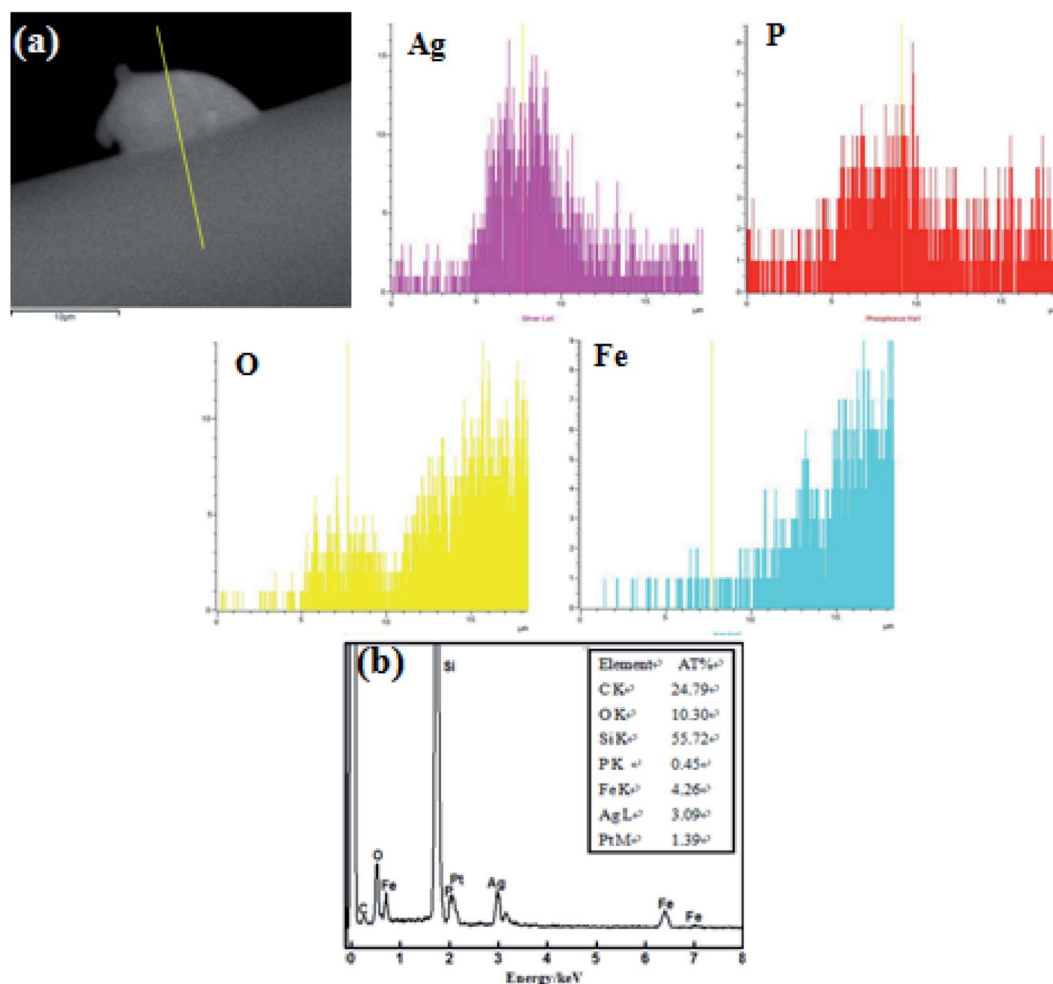
**Fig. 5**  EDS line scanning across the $Ag_3PO_4/\alpha$-$Fe_2O_3$ hybrid (a) and its EDS spectrum (b).

reflectance spectroscopy. Fig. 6(a) shows the UV-Vis diffuse reflectance absorption spectra of pure $Ag_3PO_4$, $\alpha$-$Fe_2O_3$ and $Ag_3PO_4/\alpha$-$Fe_2O_3$ complex (1 : 2). It can be seen from Fig. 6(a) that the maximum light absorption band edges of pure $Ag_3PO_4$ and $\alpha$-$Fe_2O_3$ are about 550 nm and 650 nm, respectively. Compared with pure $Ag_3PO_4$, the absorption wavelength of the $Ag_3PO_4/\alpha$-$Fe_2O_3$ hybrid photocatalyst in the visible light region has a red shift, which enhances the visible



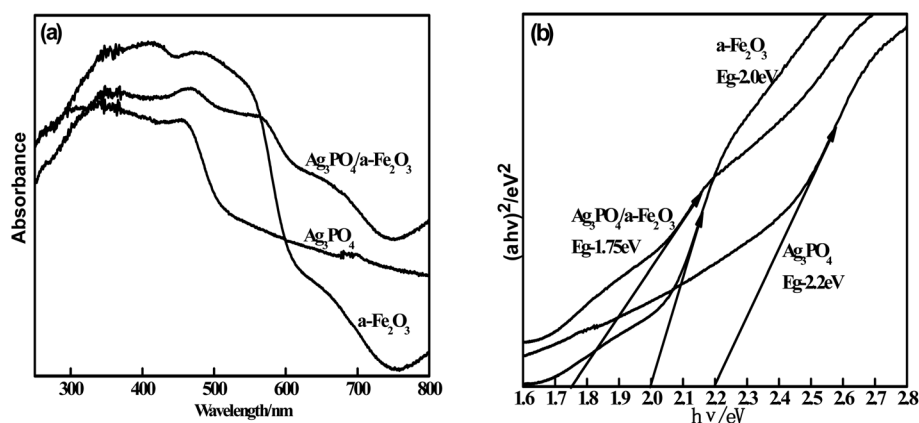**Fig. 6**  UV-Vis spectra (a) and the corresponding $(\alpha h\nu)^2$–$h\nu$ curve of the $Ag_3PO_4$, $\alpha$-$Fe_2O_3$ and $Ag_3PO_4/\alpha$-$Fe_2O_3$ hybrid(b).

light response range thus increasing the utilization rate of light. The red-shift phenomenon is attributed to the hetero-junction structure formed between $Ag_3PO_4$ and $\alpha$-$Fe_2O_3$ which may be induced by the structural defects, and the enhanced internal stress results in the overlap of the electron wave function generated in the process. From the $(\alpha h\nu)^2 \sim h\nu$ curve in Fig. 6(b), it can be concluded that the $E_g$ values of $Ag_3PO_4$ and $\alpha$-$Fe_2O_3$ are about 2.2 eV and 2.0 eV, respectively.[27,28] The valence band $E_{VB}$ and conduction band position $E_{CB}$ can be obtained from the calculation formula of the semiconductor energy band structure:[29]

$$E_{VB} = X - E^e + 0.5E_g \qquad (1)$$

$$E_{CB} = E_{VB} - E_g \qquad (2)$$

$X$ is the absolute electronegativity of the semiconductor, and the $X$ values of $Ag_3PO_4$ and $\alpha$-$Fe_2O_3$ are 6.20 eV and 5.87 eV, respectively; $E^e$ is the energy of a free electron on the hydrogen scale (about 4.5 eV). Therefore, the $E_{VB}$ and $E_{CB}$ of $Ag_3PO_4$ are 2.80 eV and 0.60 eV, and the $E_{VB}$ and $E_{CB}$ of $\alpha$-$Fe_2O_3$ are 2.37 eV and 0.37 eV, respectively.

The photocatalytic activity of $Ag_3PO_4$, $\alpha$-$Fe_2O_3$ and $Ag_3PO_4$/$\alpha$-$Fe_2O_3$ hybrid photocatalyst for rhodamine B degradation under visible light was investigated. It can be seen from Fig. 7(a) that rhodamine B hardly degrades itself. At the same time, the degradation efficiency of pure $Ag_3PO_4$ and $\alpha$-$Fe_2O_3$ for rhodamine B was 82% and 8%, respectively, after 10 min of visible light catalysis. It can be clearly seen from Fig. 7(b) that, compared with pure $\alpha$-$Fe_2O_3$, the photocatalytic degradation effect of rhodamine B by loading $Ag_3PO_4$ on $\alpha$-$Fe_2O_3$ has been greatly improved. With the increase in the $Ag_3PO_4$ load, the catalytic activity of the $Ag_3PO_4$/$\alpha$-$Fe_2O_3$ hybrid photocatalyst first increased and then decreased. When the molar ratio of $Ag_3PO_4$ to $\alpha$-$Fe_2O_3$ was 1 : 2, the catalytic degradation ability of rhodamine B solution was the best, and the catalytic degradation efficiency reached 95% after 10 min. Combined with the SEM images of $Ag_3PO_4$/$\alpha$-$Fe_2O_3$ hybrids with different ratios shown in Fig. 4, it can be predicted that when the composite ratios of $Ag_3PO_4$ and $\alpha$-$Fe_2O_3$ are 1 : 4 and 1 : 3, fewer $Ag_3PO_4$ particles are loaded on the sheet $\alpha$-$Fe_2O_3$, which is unfavorable to the migration of photoelectric charge carriers between the two and hence unfavorable to the improvement of photocatalytic activity. When the composite ratio of $Ag_3PO_4$ and $\alpha$-$Fe_2O_3$ is 1 : 2, the distribution of $Ag_3PO_4$ particles on the sheet $\alpha$-$Fe_2O_3$ is more uniform, which improves the dispersion of $Ag_3PO_4$ particles and increases the photocatalytic specific surface area. The heterojunction structure formed between $Ag_3PO_4$ and $\alpha$-$Fe_2O_3$ effectively promoted the separation of photogenerated electrons and holes and improved the electron migration efficiency, thus improving the photocatalytic activity of the material.[30,31] However, too much $Ag_3PO_4$ will cause $Ag_3PO_4$ particles to agglomerate on the sheet $\alpha$-$Fe_2O_3$, which will reduce the surface activity of $Ag_3PO_4$/$\alpha$-$Fe_2O_3$, thus reducing the photocatalytic activity of the composite photo-catalyst. At the same time, it can be seen that the catalytic activity of the $Ag_3PO_4$/$\alpha$-$Fe_2O_3$ hybrid photocatalyst is higher
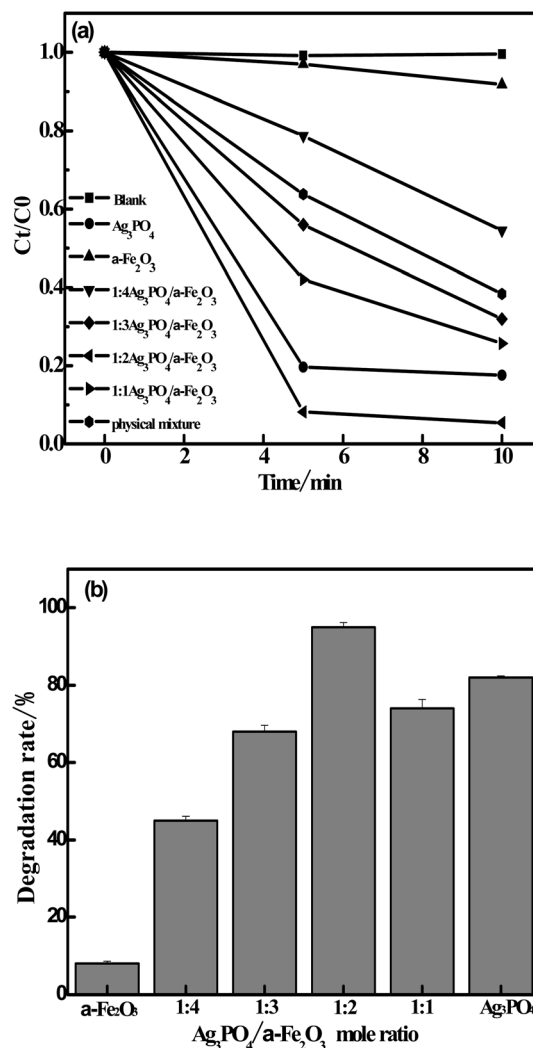


Fig. 7 Kinetic curves of degradation of rhodamine B (a); photocatalytic degradation curves of RhB solution by different catalyst samples (b).

than that of the physical mixture with the same proportion, which further indicates that the $Ag_3PO_4$/$\alpha$-$Fe_2O_3$ hybrid pho-tocatalyst prepared in this experiment formed a hetero-junction structure and improved the photocatalytic activity, while the simple physical mixture cannot form a hetero-junction structure.

The possible mechanism of the photocatalytic degradation of rhodamine B by the $Ag_3PO_4$/$\alpha$-$Fe_2O_3$ hybrid photocatalyst is shown in Fig. 8. Under simulated solar irradiation, because the gap width of $Ag_3PO_4$ and $\alpha$-$Fe_2O_3$ is narrow, and the absorb-ability is good in the range of visible wavelength, the electrons in the valence band are easily excited to transition to the conduction band, while the holes remain in the valence band. First, the $E_{CB}$ (0.60 eV) of $Ag_3PO_4$ is higher than that of $\alpha$-$Fe_2O_3$ (0.37 eV), and the photogenerated electrons in the $\alpha$-$Fe_2O_3$ conduction band can easily migrate to the $Ag_3PO_4$ conduction band. The $E_{VB}$ of $Ag_3PO_4$ (2.80 eV) is higher than that of $\alpha$-$Fe_2O_3$ (2.37 eV), and the valence band holes of $Ag_3PO_4$ are transferred to the valence band of $\alpha$-$Fe_2O_3$; thus, the photogenerated
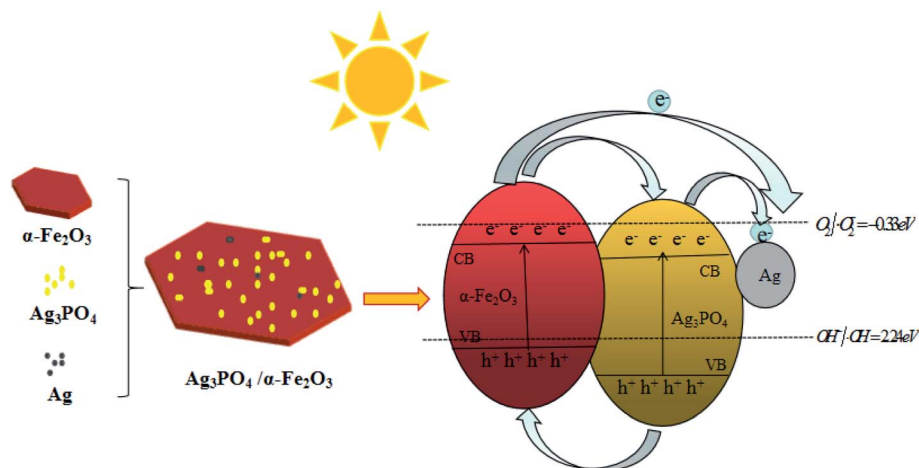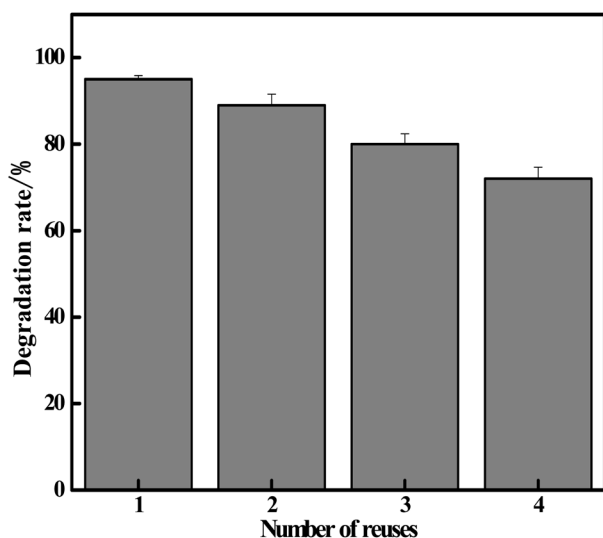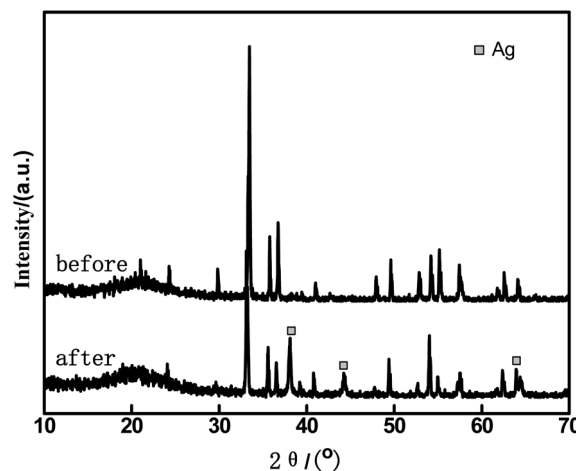
Fig. 8 Mechanism of enhanced photocatalytic activity.



Fig. 9 Effect of reuse times of the $Ag_3PO_4/\alpha$-$Fe_2O_3$ hybrid catalyst on RhB degradation rate.

catalytic degradation rate is that a small amount of elemental silver (Ag) is produced by the photocorrosion of $Ag_3PO_4$ during the degradation process.[32] Meanwhile, the loss of some amount catalyst in the processes of washing and recycling is also a reason for the reduction in the degradation rate.

Fig. 11 shows the UV-Vis absorption spectra of the $Ag_3PO_4/\alpha$-$Fe_2O_3$ photocatalytic degradation of rhodamine B. It can be seen from Fig. 11 that with the extension of the photocatalytic degradation time, the absorption peak intensity of rhodamine B solution gradually decreased, and rhodamine B was almost completely degraded after 10 min. In the whole process of photocatalytic degradation, the position and shape of the absorption peak of rhodamine B did not change, and no new absorption peak was generated, indicating that the concentration of rhodamine B only decreased in the degradation process, and no new substances were generated. Finally, it was concluded that rhodamine B might be catalyzed to degrade to $H_2O$ and $CO_2$.

electron–hole pair is effectively separated. Second, $Ag_3PO_4$ will produce a small amount of Ag due to the photocorrosion phenomenon, which can further capture electrons from the conduction band of $Ag_3PO_4$ and $\alpha$-$Fe_2O_3$, thus promoting the separation of photogenerated electrons and holes, and enhancing the photocatalytic activity.

Fig. 9 shows the effect of repeated usage times of the $Ag_3PO_4/\alpha$-$Fe_2O_3$ hybrid catalyst on the degradation rate of rhodamine B. It can be seen from Fig. 9 that the photocatalytic degradation rate of rhodamine B decreased from 95% to 72% after repeated use of the $Ag_3PO_4/\alpha$-$Fe_2O_3$ hybrid catalyst for four times. The photocatalytic degradation rate decreased slightly, but the photocatalyst still had certain stability and could be reused many times. According to the XRD comparison patterns of the $Ag_3PO_4/\alpha$-$Fe_2O_3$ hybrid catalyst before and after use in Fig. 10, it can be clearly seen that the main reason for the decrease in the



Fig. 10 XRD patterns of the $Ag_3PO_4/\alpha$-$Fe_2O_3$ hybrid catalyst before and after application.
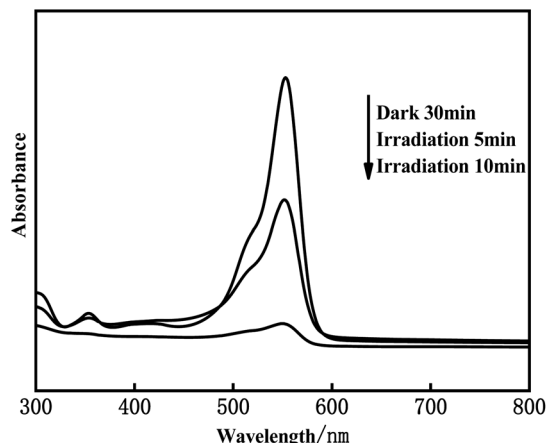
**Fig. 11** UV-Vis spectra of Ag$_3$PO$_4$/α-Fe$_2$O$_3$ photocatalytic degradation of rhodamine B.

## 4. Conclusion

Based on a series of experiments and characterization, the following conclusions are drawn: when the molar ratio of Ag$_3$PO$_4$ to α-Fe$_2$O$_3$ is 1 : 2, the catalytic degradation of the rhodamine B solution was the highest, and the catalytic degradation efficiency reached 95% in 10 min, which was significantly higher than that of pure Ag$_3$PO$_4$ and α-Fe$_2$O$_3$. This may be because the small Ag$_3$PO$_4$ particles are uniformly dispersed on the α-Fe$_2$O$_3$ sheet structure, which increases the catalytic specific surface area of Ag$_3$PO$_4$ particles. Moreover, Ag$_3$PO$_4$ particles and α-Fe$_2$O$_3$ sheets were closely combined to form a heterojunction structure, which improved the migration of photogenerated electrons and holes between the two. Thus, the photocatalytic activity of Ag$_3$PO$_4$/α-Fe$_2$O$_3$ hybrids was improved. The Ag$_3$PO$_4$/α-Fe$_2$O$_3$ hybrids had good visible light catalytic activity and stability, and could be reused many times.

## Author contributions

Y. Gao and C. M. Gui contributed to the conception and design of the work. H. D Ma, L. C. Han planned and designed the experiments, and made data acquisition. C. M. Gui, Y. Gao, H. D Ma, L. C. Han and H. C. Deng contributed to the analysis, data interpretation characterizing the samples. All authors have reviewed and approved to the final version of the manuscript.

## Conflicts of interest

The authors declare that they have no known competing financial interests or personal relationships that could have appeared to influence the work reported in this paper.

## Acknowledgements

## References

1 Q. Li, T. Shi, X. Li, K. G. Lu, M. Li, F. L. Liu, H. G. Li and M. Lei, *Appl. Catal., B*, 2018, **229**, 8.

2 J. J. Huang, W. P. Wu, R. X. Zhang, G. Q. Lu, B. Chen, Z. M. Chen and C. M. Gui, *Nano Energy*, 2002, **92**, 106734.

3 R. C. Shen, C. J. Jiang, Q. J. Xiang, J. Xie and X. Li, *Appl. Surf. Sci.*, 2019, **471**, 43.

4 J. J. Huang, L. L. Xu, D. F. Zhao, J. Wang, C. R. Chu, H. D. Chen, Y. H. Liu and Z. M. Che, *Chem. Eng. J.*, 2020, **383**, 123199.

5 M. J. Nalbandian, M. Zhang, J. Sanchez, S. Kim, Y.-H. Choa, D. M. Cwiertny and N. V. Myung, *J. Hazard. Mater.*, 2015, **299**, 141.

6 L. Cui, S. L. Liu, F. K. Wang, J. Y. Li, Y. H. Song, Y. Sheng and H. F. Zou, *J. Alloys Compd.*, 2020, **826**, 154001.

7 J. Singh, S. A. Khan, J. Shah, R. K. Kotnala and S. Mohapatra, *Appl. Surf. Sci.*, 2017, **422**, 953.

8 R. K. Nainani and P. Thakur, *Water Sci. Technol.*, 2016, **73**, 1927.

9 Y. Lyu, F. Wei, T. Zhang, L. Luo, Y. Pan, X. Yang, H. Yu and S. Zhou, *J. Alloys Compd.*, 2021, **876**, 160016.

10 Y. J. Lee, J. K. Kang, S. J. Park, C. G. Lee, J. K. Moon and P. J. J. Alvarez, *Chem. Eng. J.*, 2020, **402**, 126183.

11 Y. Ma, J. Li, Y. Jin, K. Gao, H. Cai and G. Ou, *Chemosphere*, 2021, **285**, 131440.

12 Z. Hu, J. Lyu and M. Ge, *Mater. Sci. Semicond. Process.*, 2020, **105**, 104731.

13 J. Wang, X. Yu, X. Fu, Y. Zhu and Y. Zhang, *Mater. Sci. Semicond. Process.*, 2021, **121**, 105329.

14 J. G. Du, Z. Xu, H. Li, H. J. Yang, S. J. Xu, J. Wang, Y. A. Jia, S. L. Ma and S. H. Zhan, *Appl. Surf. Sci.*, 2021, **541**, 148487.

15 Z. Y. Wu, J. P. Yu, W. F. Wang, C. H. X. H. Xin, X. Yu and Y. T. Tang, *J. Alloy. Compd.*, 2021, **891**, 161877.

16 Z. Jiang, W. Wan, H. Li, S. Yuan, H. Zhao and P. K. Wong, *Adv. Mater.*, 2018, **30**, 1706108.

17 Y. Geng, D. Chen, N. Li, Q. Xu, H. Li, J. He and J. Lu, *Appl. Catal., B*, 2021, **280**, 119409.

18 W. Wang, W. Zhao, H. Zhang, X. Dou and H. Shi, *Chin. J. Catal.*, 2021, **42**(1), 97.

19 P. Wu, X. Zhao, C. Li, M. Yang, G. Li, S. Zhang, J. Ming, M. Liu, Z. Qian and P. Fang, *New J. Chem.*, 2020, **44**, 16370.

20 W. Su, X. Liu, L. Tan, Z. Cui, Y. Liang, Z. Li, S. Zhu and S. Wu, *ACS Sustain. Chem. Eng.*, 2020, **8**, 2577.

21 M. Liu, X. Xue, S. Yu, X. Wang, X. Hu, H. Tian, H. Chen and W. Zheng, *Sci. Rep.*, 2017, 7, 3637.

22 J. Xu, X. Li, J. Niu, M. Chen, J. Yue and J. Alloy, *Compd*, 2020, **834**, 155061.

23 P. F. Wang, P. H. Shi, Y. C. Hong, X. J. Zhou and W. F. Yao, *Mater. Res. Bull.*, 2015, **62**, 24.

24 L. Luo, Y. Li, J. Hou and Y. Yang, *Appl. Surf. Sci.*, 2014, **319**, 332.

25 P. Shao, Z. Ren, J. Tian, S. Gao, X. Luo, W. Shi, B. Yan, J. Li and F. Cui, *Chem. Eng. J.*, 2017, **323**, 64.

26 V. G. Deshmane, S. L. Owen, R. Y. Abrokwah and D. Kuila, *J. Mol. Catal. A: Chem.*, 2015, **408**, 202.

27 M. Q. Wen, T. Xiong, Z. G. Zang, W. Wei, X. T. Tang and F. Dong, *Opt. Express*, 2016, **24**, 10205.

28 D. Y. Liang, C. Cui, H. H. Hu, Y. P. Wang, S. Xu, B. L. Ying, P. G. Li, B. Q. Lu and H. L. Shen, *J. Alloys Compd.*, 2014, **582**, 236.

29 M. Wang, P. Y. Guo and G. J. Yang, *Mater. Lett.*, 2017, **192**, 96.

30 P. Kang, L. Zhang, B. Cheng and J. Yu, *Appl. Catal., B*, 2017, **218**, 570.

31 A. Liu, C. Zhang, Y. Zhu, K. Li, J. Huang, Y. K. Du and P. Yang, *J. Colloid Interface Sci.*, 2019, **535**, 408.

32 M. Ge, N. Zhu and N. Y. P. Zhao, *Ind. Eng. Chem. Res.*, 2012, **51**, 5167.